



HAL
open science

LiNbO₃-type InFeO₃: Room-temperature polar magnet without second-order Jahn-Teller active ions

K. Fujita, T. Kawamoto, I. Yamada, O. Hernandez, N. Hayashi, H. Akamatsu, W. Lafargue-Dit-Hauret, X. Rocquefelte, M. Fukuzumi, P. Manuel, et al.

► **To cite this version:**

K. Fujita, T. Kawamoto, I. Yamada, O. Hernandez, N. Hayashi, et al.. LiNbO₃-type InFeO₃: Room-temperature polar magnet without second-order Jahn-Teller active ions. *Chemistry of Materials*, 2016, 28 (18), pp.6644–6655. 10.1021/acs.chemmater.6b02783 . hal-01381124

HAL Id: hal-01381124

<https://univ-rennes.hal.science/hal-01381124>

Submitted on 2 Feb 2017

HAL is a multi-disciplinary open access archive for the deposit and dissemination of scientific research documents, whether they are published or not. The documents may come from teaching and research institutions in France or abroad, or from public or private research centers.

L'archive ouverte pluridisciplinaire **HAL**, est destinée au dépôt et à la diffusion de documents scientifiques de niveau recherche, publiés ou non, émanant des établissements d'enseignement et de recherche français ou étrangers, des laboratoires publics ou privés.

LiNbO₃-type InFeO₃: Room-Temperature Polar Magnet without Second-Order Jahn–Teller Active Ions

Koji Fujita^{1*}, Takahiro Kawamoto¹, Ikuya Yamada^{2,3}, Olivier Hernandez⁴, Naoaki Hayashi⁵, Hirofumi Akamatsu^{6†}, William Lafargue-Dit-Hauret⁴, Xavier Rocquefelte⁴, Masafumi Fukuzumi⁷, Pascal Manuel⁸, Andrew J. Studer⁹, Christopher S. Knee¹⁰, and Katsuhisa Tanaka¹

¹Department of Material Chemistry, Graduate School of Engineering, Kyoto University, Katsura, Nishikyo-ku, Kyoto 615-8510, Japan

²Nanoscience and Nanotechnology Research Center, Osaka Prefecture University, 1-2 Gakuen-cho, Sakai, Osaka 599-8531, Japan

³Precursory Research for Embryonic Science and Technology, Japan Science and Technology Agency, Tokyo 102-0075, Japan

⁴Institut des Sciences Chimiques de Rennes, UMR CNRS 6226, Université de Rennes 1, 263 Avenue du Général Leclerc, 35042 Rennes, France

⁵Research Institute for Production Development, Shimogamo-Morimoto-cho 15, Sakyo-ku, Kyoto 606-0805, Japan

⁶Materials Research Institute and Department of Materials Science and Engineering, Pennsylvania State University, University Park, Pennsylvania, 16802, USA

⁷Department of Project Management, Hyogo Prefectural Institute of Technology, 3-1-12 Yukihiro-cho, Suma-ku, Kobe 645-0037, Japan

⁸ISIS Facility, STFC Rutherford Appleton Laboratory, Harwell Science and Innovation Campus, Oxon OX11 0QX, United Kingdom

⁹Bragg Institute, Australian Nuclear Science and Technology Organisation, Locked Bag 2001, Kirrawee DC, NSW 2232, Australia

¹⁰Environmental Inorganic Chemistry, Department of Chemistry and Chemical Engineering, Chalmers University of Technology, SE-412 96, Gothenburg, Sweden

ABSTRACT: Great effort has been devoted to developing single-phase magnetoelectric multiferroics, but room-temperature coexistence of large electric polarization and magnetic ordering still remains elusive. Our recent finding shows that such polar magnets can be synthesized in small-tolerance-factor perovskites $A\text{FeO}_3$ with unusually small cations at the A -sites, which are regarded as having a LiNbO₃-type structure (space group $R3c$). Herein, we experimentally reinforce this finding by preparing a novel room-temperature polar magnet, LiNbO₃-type InFeO₃. This compound is obtained as a metastable quench product from an orthorhombic perovskite phase stabilized at 15 GPa and an elevated temperature. The structure analyses reveal that the polar structure is characterized by displacements of In³⁺ (d^{10}) and Fe³⁺ (d^5) ions along the hexagonal c -axis (pseudocubic [111] axis) from their centrosymmetric positions, in contrast to well-known perovskite ferroelectrics (e.g., BaTiO₃, PbTiO₃, BiFeO₃) where d^0 transition-metal ions and/or $6s^2$ lone-pair cations undergo polar displacements through the so-called second-order Jahn–Teller (SOJT) distortions. Using density functional theory calculations, the electric polarization of LiNbO₃-type InFeO₃ is estimated to be 96 $\mu\text{C}/\text{cm}^2$ along the c -axis, comparable to that of an isostructural and SOJT-active perovskite ferroelectric, BiFeO₃ (90–100 $\mu\text{C}/\text{cm}^2$). Magnetic studies demonstrate weak ferromagnetic behavior at room temperature, as a result of the canted G-type antiferromagnetic ordering of Fe³⁺ moments below $T_N \sim 545$ K. The present work shows functional versatility of small-tolerance-factor perovskites and provides a useful guide for the synthesis and design of room-temperature polar magnets.

INTRODUCTION

The search for single-phase materials combining a spontaneous magnetization and a large electric polarization above room temperature is an important direction in order to develop novel spintronic and memory devices. As for transition metal perovskite oxides ABO_3 , magnets usually require partially filled d shells of transition metals on the B -site to form localized magnetic moments, whereas d^0 B -site cations are a common source of polar structural distortions that lead to electric polarizations. Because of the conflict of electronic configuration requirements, $6s^2$ lone

pair cations such as Pb²⁺ and Bi³⁺ on the A -site are often utilized to induce the polar structures in magnets. Until recently, however, rhombohedral perovskite-type BiFeO₃ and related compounds (space group $R3c$) are only known to possess both magnetic and dielectric orders at room temperature^{1,2}: bulk BiFeO₃ exhibits G-type antiferromagnetic order with an incommensurate spin-cycloidal structure ($T_N \sim 643$ K)^{3,4} and ferroelectricity ($T_c \sim 1103$ K)^{5,6}; this magnetic structure leads to zero macroscopic magnetization, but cation substitutions^{7,8} or strained thin films^{9–11} suppress the cycloidal modulation to induce

a macroscopic magnetization due to a canting of the antiferromagnetically ordered Fe^{3+} spins, so-called weak ferromagnetism. The scarcity of the multiferroic phases at room temperature has stimulated a lot of theoretical and experimental work aimed at disclosing mechanisms to design polar magnets without utilizing d^0 or $6s^2$ cations. Examples include extremely small tolerance factors,¹² spin spirals,^{13,14} charge ordering,¹⁵ and geometric improper and hybrid improper ferroelectricity.^{16,17}

Among these mechanisms, ABO_3 perovskites with very small tolerance factors, t , as defined by $t = (r_A + r_O) / (\sqrt{2}(r_B + r_O))$, where r_A , r_B , and r_O stand for the ionic radii of A -site, B -site and O^{2-} ions, respectively, have recently attracted much attention because they possess robust polar structures (typically above $50 \mu\text{C}/\text{cm}^2$) and allow incorporation of different magnetic transition-metal ions in both the A - and B -sites.^{18–42} These perovskites contain unusually small A -site cations and crystallize in noncentrosymmetric polar space group $R3c$. The $R3c$ structure is derived from the cubic aristotype by a combination of a notable magnitude of antiferrodistortive tilts of the BO_6 octahedra about the pseudocubic [111] axis ($\bar{a}\bar{a}\bar{a}$ in Glazer notation^{43,44}) and the polar displacement of A -site cations along the same axis.⁴⁵ Thus, it can be viewed as a grossly distorted rhombohedral perovskite structure, often called a LiNbO_3 -type structure. Note that although the crystal symmetry of LiNbO_3 -type compounds is the same as that of BiFeO_3 , their crystal structures are different from each other with respect to the magnitude of tilting angle, φ , about the pseudocubic [111] axis (or equivalently, the c -axis in the hexagonal setting); $\varphi = 13.8^\circ$ for BiFeO_3 ,⁴⁶ whereas LiNbO_3 -type compounds have $\varphi > 20^\circ$ due to the extremely small tolerance factors.⁴⁷ To stabilize the strongly tilted BO_6 octahedral framework in the LiNbO_3 -type structure, high-pressure and high-temperature conditions are often required.

As a result of materials exploration using the high-pressure synthesis technique, it is now possible to create a number of LiNbO_3 -type and related polar magnets.^{18,19,29–36,38–41,48,49} In addition, the polar structural distortion in the magnetic ordered phases was predicted to induce weak ferromagnetism through the Dzyaloshinsky–Moriya (DM) interaction,^{50,51} leading to a proposed mechanism for the electric field control of magnetization.⁵² Despite these major developments, however, above-room-temperature magnetic ordering was rarely observed for LiNbO_3 -type magnets. To address this issue, we set out to study a series of small-tolerance-factor $A\text{FeO}_3$ perovskites that have potentially strong magnetic interactions in the Fe^{3+} sublattice. Along this research direction, we have recently fabricated a room-temperature polar magnet, LiNbO_3 -type ScFeO_3 , by locating small Sc^{3+} ions at the A -site,³⁹ although rare-earth ferrites with a larger rare-earth R^{3+} ion ($R = \text{La–Lu}$ or Y) occupying the A -site are known to be nonpolar with an orthorhombic perovskite-type structure (space group $Pnma$).^{53,54} The magnetic studies on LiNbO_3 -type ScFeO_3 revealed weak ferromagnetism up to $T_N = 545 \text{ K}$ as a result of a canted G-type antiferromagnetic ordering of Fe^{3+} spins. This finding suggests that incorporating a small cation in the A -site of $A^{3+}\text{Fe}^{3+}\text{O}_3$ perovskites provides an avenue to design “room-temperature” polar magnets. To confirm the generality of this idea, we here focus on an $A = \text{In}$ analog, i.e., InFeO_3 . Since the ionic radius of In^{3+} (0.800 Å for 6-fold coordination⁵⁵) is much smaller than those of R^{3+} ($R = \text{La–Lu}$ or Y) ranging from 1.032 Å to 0.861 Å, it is anticipated that InFeO_3 favors a polar structural distortion as far as the perovskite-type structure is retained.

In this paper, we report on the high-pressure synthesis of a new polar magnet with $R3c$ symmetry, LiNbO_3 -type InFeO_3 . According to early studies, InFeO_3 crystallizes in the YAlO_3 -type structure (space group $P6_3/mmc$) under ambient conditions⁵⁶ and

adopts the corundum-type structure (space group $R\bar{3}c$) at 6 GPa and 1200 °C.^{57,58} Here, we demonstrate successful synthesis of the $R3c$ phase by using higher pressure (~15 GPa) at elevated temperature (above 1000 °C). The structural analyses and magnetic and optical characterizations prove the validity of our idea, i.e., the coexistence of polar structural distortion and weak ferromagnetism at room temperature. We make some structural comparisons between $R3c$ InFeO_3 and related compounds, which are of relevance to their physical properties. The mechanism of inversion symmetry breaking in $R3c$ InFeO_3 is of particular interest because there are neither d^0 nor $6s^2$ cations. Thus, the Born effective charges and electric polarization are evaluated by using the density functional theory (DFT) calculations to examine the origin of polar structural distortion. We also estimate the magnetocrystalline anisotropy energy using the DFT calculations to obtain an insight into the magnetic structure. The overall results indicate that $R3c$ InFeO_3 is a promising candidate as a room-temperature magnetoelectric material.

2. EXPERIMENTAL SECTION

Polycrystalline InFeO_3 was prepared by the solid-state reaction under high pressure and high temperature. Reagent-grade In_2O_3 (99.999 %, Kojundo Chemical) and Fe_2O_3 (99.99 %, Kojundo Chemical) were used as starting materials. The stoichiometric mixture of In_2O_3 and Fe_2O_3 powders was first ground in an agate mortar. The powder mixture was then placed into a Pt capsule and put into a high-pressure cell. The high-pressure and high-temperature treatment was performed at 15 GPa and 1450 °C using a Kawai-type high-pressure apparatus. After being treated for 30 min, the sample was cooled to room temperature in a few minutes, and the pressure was slowly released.

Synchrotron X-ray diffraction (SXRD) data were collected at room temperature using a large Debye-Scherrer camera with an imaging-plate-type detector, installed in the BL02B2 beamline at SPring-8. The incident beam was monochromated at $\lambda = 0.65014 \text{ \AA}$. The finely ground powder sample was housed in a Lindemann glass capillary tube with an inner diameter of 0.2 mm and was continuously rotated during measurements to reduce the effect of preferential orientation. The structural parameters were refined by the Rietveld analysis⁵⁹ using the FullProf program.⁶⁰ In the refinement, an absorption correction was applied using $\mu_r = 0.7$.⁶¹ *In-situ* SXRD was measured under high pressure and high temperature using a Kawai-type apparatus SPEED-1500 installed in the BL04B1 beamline at SPring-8.⁶² White X-ray was used as the incident beam and a solid-state germanium detector was utilized for data collection. The X-rays diffracted from the sample were collected at a fixed 2θ angle of about 5° by the energy dispersive method. MgO sleeve, in which the sample was enclosed, was used as the pressure marker; that is, the applied pressure was evaluated from the lattice parameters of MgO using an equation of state.⁶³ Variable-temperature neutron powder diffraction (NPD) data were recorded using the time-of-flight (TOF) diffractometer WISH at ISIS neutron facility⁶⁴ and the high-intensity powder diffractometer WOMBAT ($\lambda = 2.41351 \text{ \AA}$) at ANSTO’s OPAL facility. A 40-mg sample was put in an evacuated vanadium can for the experiments on WISH, while a 100-mg sample was inserted in a He-filled vanadium can for the measurements on WOMBAT. The nuclear and magnetic structures were refined by the Rietveld analysis using the FullProf suite⁶⁰ and drawn by VESTA.⁶⁵

A second-harmonic generation (SHG) response was examined at room temperature using a pulsed Nd:YAG laser (λ : 1064 nm, pulse duration: 25 ps, repetition rate: 10 Hz) as the light source. Magnetization data were obtained with a SQUID magnetometer

(Quantum Design, MPMS). The magnetic-field dependence of magnetization was measured at 5 and 300 K. ^{57}Fe Mössbauer spectroscopy was performed in a transmission geometry using a $^{57}\text{Co/Rh}$ radiation source at various temperatures. The calibration for a velocity scale was referred to $\alpha\text{-Fe}$ foil measured at room temperature.

To estimate the Born effective charges and electric polarization, the first-principles calculations were performed using the projector augmented-wave (PAW) method^{66,67} and the PBEsol functional⁶⁸ as implemented in the VASP code.^{69,70} The PAW data sets with radial cutoffs of 1.7, 1.2 and 0.8 Å for In, Fe, and O, respectively, were used with a plane-wave cutoff energy of 700 eV. The following states were described as valence electrons: $4d$, $5s$ and $5p$ for In; $3p$, $3d$, $4s$ for Fe; and $2s$, $2p$ for O. We assumed a centrosymmetric $R\bar{3}c$ perovskite-type structure as a higher-symmetry parent structure. Γ -centered k -point mesh sampling of $6 \times 6 \times 4$ was used for the 30-atom conventional hexagonal unit cell. The lattice constants and internal coordinates were optimized under the constraint of the symmetry until the residual stress and force converged to less than 0.003 GPa and 0.001 eV/Å, respectively. According to our experimental results (see section 3.4), we employed a G-type antiferromagnetic configuration where the Fe spins are aligned ferromagnetically within the layers and antiferromagnetically between the layers. The Born effective charge tensor of atom s , Z_{ss}^* , in the parent $R\bar{3}c$ structure was calculated by density functional perturbation theory, and the total electric polarization for the polar $R3c$ structure was derived from the following equation,⁷¹

$$P = \frac{e}{V} \sum_s Z_{ss}^* u_s$$

where e is the elementary charge, V is the unit-cell volume, and u_s is the displacement of atom s away from its position in the $R\bar{3}c$ structure. To explore the magnetic structure, we also calculated the magnetocrystalline anisotropy energy using the spin-orbit coupling implementation of DFT. The calculation method is detailed in Supporting Information (SI), section S1.

3. RESULTS

3.1 Crystal Structure Analysis. Figure 1a shows the room-temperature SXR D pattern of sample recovered to ambient conditions from 15 GPa and 1450 °C, together with the result of the Rietveld refinement. The diffraction pattern can be indexed in rhombohedral symmetry. Considering the reflection conditions in the (obverse) hexagonal setting ($-h + k + l = 3n$ for $hkil$, $h + l = 3n$ and $l = 2n$ for $h\bar{h}0l$, $l = 3n$ for $h\bar{h}2\bar{h}l$, and $l = 6n$ for $000l$ (n : integer)), the possible space group is either noncentrosymmetric polar $R3c$ or centrosymmetric nonpolar $R\bar{3}c$. A small amount of unknown phases is observed with intensities less than 2% of the main peak of the rhombohedral phase (Figure S1). The $R3c$ phase possesses a completely ordered arrangement of A - and B -site cations, whereas the $R\bar{3}c$ phase is characterized by their disordered arrangement. Because of the large X-ray scattering contrast between In and Fe atoms, SXR D analysis should give accurate information about the cation occupancy in the rhombohedral phase. Rietveld refinement was carried out with the cation-ordered LiNbO_3 -type structure (polar $R3c$), with In atoms placed at $6a$ site (0, 0, z), Fe atoms at $6a$ (0, 0, 0), and O atoms at $18b$ (x , y , z), and also with the cation-disordered corundum-type structure (centrosymmetric $R\bar{3}c$), with In/Fe atoms placed at $12c$ site (0, 0, z) and O atoms at $18e$ (x , $1/3$, $1/12$). The refinement with the LiNbO_3 -type $R3c$ model yields a much better fit ($R_{\text{wp}} = 10.6\%$ and $R_{\text{B}} = 2.9\%$) when compared to the

corundum-type $R\bar{3}c$ model ($R_{\text{wp}} = 31.5\%$ and $R_{\text{B}} = 20.0\%$). We also checked SHG activity on the powder sample with an average particle size of 25 μm (Figure S2) and observed an intense SHG response indicative of the presence of the noncentrosymmetric

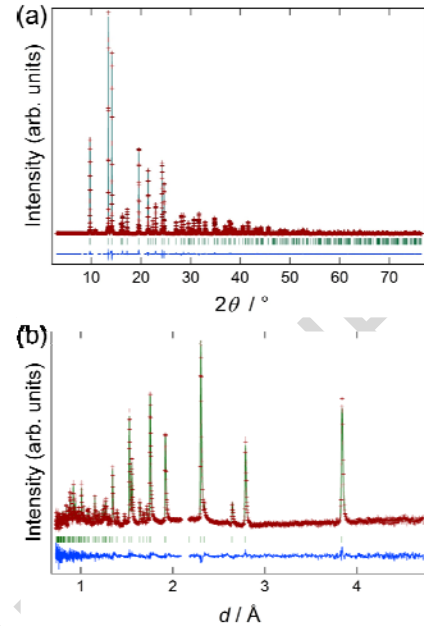


Figure 1. Rietveld refinement of (a) SXR D data at room temperature ($\lambda = 0.65014$ Å) and (b) TOF NPD data at 600 K (bank 2 data, $2\theta = 121.68^\circ$) for the InFeO_3 sample recovered to ambient conditions from 15 GPa and 1450 °C, showing the observed (red crosses) and calculated (green solid lines) profiles and the difference between the observed and calculated profiles (blue solid lines). The green ticks correspond to the positions of the calculated Bragg reflections for LiNbO_3 -type InFeO_3 . In panel a, unknown peaks are excluded in the refinement. In panel b, a vanadium peak at $d \sim 2.15$ Å originating from the sample holder is excluded in the refinement.

structure; the SHG intensity is approximately 3 times larger than that of α -quartz standard sieved into the same particle size range (20–45 μm). These results allow us to conclude that the rhombohedral phase has the polar $R3c$ symmetry.

Following these results, we analyzed variable-temperature NPD data recorded on WISH@ISIS and WOMBAT@ANSTO. In the analysis, the TOF NPD data on WISH were given high priority because of the better counting statistics and resolution over a wide d -range. As described in section 3.4, both nuclear and magnetic reflections are observed at temperatures up to 540 K as a result of the magnetic ordering of the Fe^{3+} sublattice. Therefore, 600 K data including only nuclear reflections were initially checked (Figure 1b). Such a high temperature may induce a transition into a parent paraelectric phase, but our attempt to refine the data with a centrosymmetric perovskite (non-corundum) $R\bar{3}c$ model,⁷² where In atoms are located on $6a$ site (0, 0, $1/4$), Fe atoms on $6b$ (0, 0, 0), and O atoms on $18e$ (x , $1/3$, $1/12$), leads to poor refinement quality ($R_{\text{wp}} = 17.0\%$ and $R_{\text{B}} = 12.3\%$). Rather, the polar $R3c$ structure provides the better fit ($R_{\text{wp}} = 11.4\%$ and $R_{\text{B}} = 4.4\%$) as shown in Figure 1b, indicating the persistence of the structural polarity even at 600 K. Since the coherent neutron scattering lengths of In (4.065×10^{-15} m) and Fe (9.450×10^{-15} m) are quite different from each other and neutrons are sensitive to oxygen, NPD should be more advantageous than SXR D for the analysis of site occupancies of InFeO_3 . When the occupancy factors of cation and anion sites in the polar $R3c$ model

are allowed to vary, they remain approximately unity at 600 K [$g(\text{In}) = 1.008(18)$, $g(\text{Fe}) = 1.012(9)$, and $g(\text{O}) = 0.991(7)$], inductively coupled plasma shows a cationic ratio of $\text{In}_{1.00}\text{Fe}_{1.06}$, consistent with the nominal composition within the expected errors. Hence, the site occupancies are fixed to the stoichiometric values in the final refinements of SXRD and NPD data. For the TOF NPD data in the temperature range of 5 to 600 K, the nuclear reflections are reasonably refined with the stoichiometric $R3c$ structure, while a magnetic structure is involved in the refinement for $T \leq 540$ K (see section 3.4).

The refined structural parameters of LiNbO_3 -type ($R3c$) InFeO_3 at selected temperatures are listed in Table 1. Hereafter, we use the structural parameters at 300 K derived from the TOF NPD analysis. The calculated density for $R3c$ InFeO_3 (6.45 g/cm^3) is significantly larger than that for the ambient-pressure phase, YAlO_3 -type ($P6_3/mmc$) InFeO_3 (6.22 g/cm^3)⁵⁶ and even larger than that for the high-pressure phase, corundum-type ($R\bar{3}c$) InFeO_3 (6.39 g/cm^3), obtained at 6 GPa and 1200 °C.⁵⁷ The bond valence sum (BVS)⁷³ calculated from the refined bond lengths is 2.92 for In and 2.79 for Fe, implying a cation formal oxidation state of $\text{In}^{3+}\text{Fe}^{3+}\text{O}_3$.

A polyhedral representation of the crystal structure refined against the TOF NPD data at 300 K is shown in Figure 2a. The In and Fe atoms occupy six-coordinated A - and B -sites to form InO_6 and FeO_6 octahedra, respectively. As expected for the LiNbO_3 -type structure, there exist the corner-shared frameworks of InO_6 and FeO_6 octahedra, which are interpenetrated via edge-sharing octahedral dimers in the ab -plane and face-sharing octahedral pairs along the c -axis. To relax a cation-cation repulsion in face-sharing octahedral pairs, In and Fe atoms are off the centers of their octahedra in opposite directions along the c -axis, generating three short and three long metal-oxygen bonds in the respective octahedron (Figure 2b). The octahedral distortion is estimated by the following

$$\Delta = 1/6 \sum_i [(\langle d_i \rangle - \langle d \rangle) / \langle d \rangle]^2$$

equation: $\Delta = 1/6 \sum_i [(\langle d_i \rangle - \langle d \rangle) / \langle d \rangle]^2$, where d_i is the individual bond length, and $\langle d \rangle$ is the average bond length. We obtain $\Delta = 18.8 \times 10^{-4}$ and 14.7×10^{-4} for InO_6 and FeO_6 octahedra, respectively. The magnitudes of their intraoctahedral distortions are comparable to those for ScO_6 ($\Delta = 6.1 \times 10^{-4}$) and FeO_6 ($\Delta = 21.0 \times 10^{-4}$) in LiNbO_3 -type ($R3c$) ScFeO_3 , respectively.³⁹ Obviously, $R3c$ InFeO_3 , as well as $R3c$ ScFeO_3 , possesses highly distorted FeO_6 octahedra as a result of off-centering of the central cation, unlike orthorhombic ($Pnma$) perovskites $R\text{FeO}_3$ with nearly regular FeO_6 octahedra ($\Delta \sim 10^{-5}$).^{53,54}

In light of the small-tolerance-factor perovskite, a structural feature of $R3c$ InFeO_3 ($t = 0.81$) manifests itself in a notable magnitude of FeO_6 octahedral tilt. The Fe-O-Fe bond angle is $\alpha = 138.7(2)^\circ$, showing a very large deviation from the ideal value of 180° . The tilting angle of FeO_6 octahedra about the c -axis (or pseudocubic $[111]$ axis) is estimated to be $\varphi = 27.3(2)^\circ$, which is close to $\varphi \sim 30^\circ$ for $R3c$ ScFeO_3 ($t = 0.79$),³⁹ but is much

indicating the fully In/Fe ordering as well as the absence of oxygen deficiency. Complementary elemental analysis using larger than $\varphi = 13.8^\circ$ for $R3c$ BiFeO_3 ($t = 0.91$).⁴⁶ Note that the tilting angles for $R3c$ InFeO_3 and ScFeO_3 with extremely small t values satisfy the condition $\varphi > 20^\circ$ as commonly observed for LiNbO_3 -type compounds.⁴⁷

Table 1. Lattice Parameters, Atomic Coordinates, Atomic Displacement Parameters, and Magnetic Moments of LiNbO_3 -Type InFeO_3 , Obtained from TOF NPD (5 K, 300 K, and 600 K) and SXRD (Room Temperature) Data.^a

| Atom | | 5 K | 300 K | 600 K | RT |
|------|--|-------------|-------------|-------------|--------------|
| | | TOF NPD | TOF NPD | TOF NPD | SXRD |
| | $a/\text{Å}$ | 5.27022(10) | 5.27633(11) | 5.28758(14) | 5.271952(14) |
| | $c/\text{Å}$ | 13.9822(4) | 14.0047(4) | 14.0462(5) | 13.99453(5) |
| In | z | 0.2169(2) | 0.2171(3) | 0.2166(3) | 0.21655(7) |
| | $100 \times U_{\text{eq}}/\text{Å}^2$ | 0.9(4) | 1.8(4) | 1.9(4) | 0.521(19) |
| Fe | $100 \times U_{\text{eq}}/\text{Å}^2$ | 2.0(2) | 2.07(17) | 2.34(19) | 0.47(4) |
| | μ/μ_B | 3.95(3) | 3.22(3) | | |
| O | x | 0.0293(10) | 0.0289(9) | 0.0271(12) | 0.0317(6) |
| | y | 0.3161(10) | 0.3149(10) | 0.3133(12) | 0.3119(5) |
| | z | 0.0992(8) | 0.1010(6) | 0.1010(6) | 0.1014(3) |
| | $100 \times U_{\text{eq}}/\text{Å}^2$ | 2.06(19) | 2.21(15) | 2.73(18) | |
| | $100 \times U_{\text{iso}}/\text{Å}^2$ | | | | 0.38(6) |
| | $R_{\text{wp}}/\%$ | 10.7 | 10.8 | 11.4 | 10.6 |
| | $R_{\text{B nuclear}}/\%$ | 4.04 | 4.19 | 4.41 | 2.92 |
| | $R_{\text{B magnetic}}/\%$ | 2.96 | 3.20 | | |
| | χ^2 | 1.54 | 1.06 | 1.09 | 3.74 |

^aHexagonal, space group $R3c$ (No. 161), $Z = 6$, with atoms in the following positions: In, $6a(0, 0, z)$; Fe, $6a(0, 0, 0)$; O, $18b(x, y, z)$. In the structure refinements, the occupancy parameters are fixed to unity for all the atoms. For TOF NPD data, the positions of all the atoms are refined with anisotropic displacement parameters U_{ij} (see Table S1). For SXRD data, the In and Fe positions are refined with U_{ij} (see Table S1), while the O position is treated with an isotropic displacement parameter U_{iso} . Equivalent isotropic displacement parameter U_{eq} is defined as one-third of the trace of the orthogonalized U_{ij} tensor. The magnetic moment μ is refined for the TOF NPD data at $T \leq 540$ K.

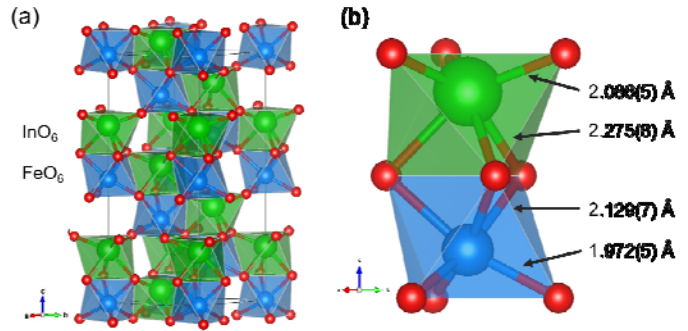


Figure 2. (a) Polyhedral representation of the crystal structure of LiNbO_3 -type InFeO_3 refined against the TOF NPD data at 300 K. Green, blue, and red spheres represent In, Fe, and O atoms, respectively. (b) Local coordination environment of InO_6 and FeO_6 octahedra stacked along the hexagonal c -axis, showing a face-sharing octahedral pair.

3.2 Estimate of Electric Polarization. Given the relative displacements of the constituent ions away from their centrosymmetric positions, it is possible to estimate the electric polarization by using the formal charges of the ions. The refined structure of $R3c$ InFeO_3 , as compared to the parent

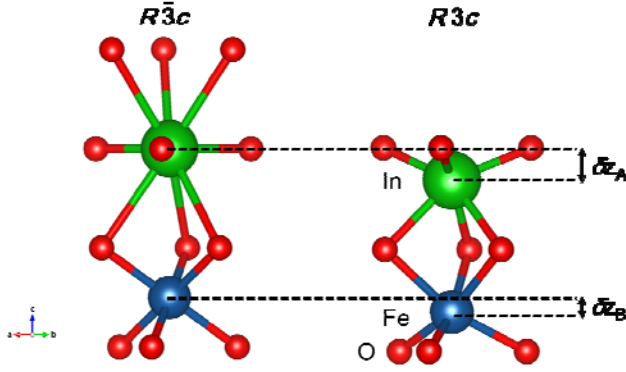


Figure 3. Polar $R3c$ structure of InFeO_3 (right) in comparison with the centrosymmetric $R\bar{3}c$ structure (left) corresponding to the rhombohedral perovskite-type structure with $a^-a^-a^-$ tilt system: green, blue, and red spheres represent In, Fe, and O atoms, respectively. In $R3c$, the displacements along the hexagonal c -axis of In and Fe atoms away from their centrosymmetric positions in the atomic coordinates are denoted as δz_A and δz_B , respectively.

tensors, Z^*_s , and the electric polarization, P_{BEC} , using DFT calculations. The obtained values of δz_A , δz_B , P_{ion} , and P_{BEC} are listed in Table 2, together with those for four other known LiNbO_3 -type ($R3c$) compounds, LiNbO_3 ,⁷⁴ ZnTiO_3 ,³⁷ ZnSnO_3 ,²⁸ and ScFeO_3 .³⁹ Table 3 presents the $Z^*_{\alpha\beta}$ tensors in Cartesian (x, y, z) coordinates for InFeO_3 , with the z -axis along the c direction, the y -axis in a gliding plane perpendicular to the a -axis, and x along a .

The electric polarization of InFeO_3 calculated by using Z^*_s is along the z -axis (or c direction) with $P_{\text{BEC}} = 96 \mu\text{C}/\text{cm}^2$, in good agreement with the corresponding value in the point charge model, $P_{\text{ion}} = 82 \mu\text{C}/\text{cm}^2$. The zz elements of Z^*_s ($Z^*_{\text{In}} = +3.51$, $Z^*_{\text{Fe}} = +3.60$, and $Z^*_O = -2.37$) are similar to their formal charges, indicating that each ion carries an effective charge close to the formal charge during the displacement. Namely, the polar structural distortion is not accompanied by charge transfer between cations and anions, suggesting the minor contribution of the second-order Jahn–Teller (SOJT) effect driven by cation-anion orbital overlap or covalency.⁷⁵ This is in striking contrast to well-known perovskite ferroelectrics (e.g., BaTiO_3 , PbTiO_3 , and BiFeO_3), where the cation-anion charge transfer causes strong SOJT distortions and hence anomalously large magnitudes of effective charges.^{76–78} One can see also from Table 2 that the main displacements in all the compounds are for the A -site cations, accompanied by the smaller B -site cation displacements in the same direction. Interestingly, InFeO_3 shares a common feature with ScFeO_3 in that the large displacement of the A -site cation, along with its high charge (+3), is significant for the sizable polarization.

3.3 Phase Transition at High Pressure and High Temperature. LiNbO_3 -type InFeO_3 provides a rare example where trivalent cation pairs are fully ordered on a single crystallographic site ($6a$ site) in the $R3c$ structure. To obtain an insight into this fact, we measured *in-situ* energy-dispersive SXRD under high-pressure and high-temperature conditions so that the phase evolution could be examined. A representative result is displayed in Figure 4. In this experiment, a stoichiometric mixture of In_2O_3 and Fe_2O_3 powders was used as the starting material. At 14.1 GPa and room temperature, two phases composed of In_2O_3 (bixbyite-type) and Fe_2O_3 (corundum-type) are detected as broad peaks in the diffraction pattern, due to the lowering of crystallinity under the high-pressure condition. As the temperature is increased to 800 °C,

centrosymmetric $R\bar{3}c$ structure,⁷² is characterized by the displacements along the hexagonal c -axis of In^{3+} and Fe^{3+} ions with respect to the surrounding oxide ions (see Figure 3). Using the formal charges of cations (+3) and their shifts along the c -axis in atomic coordinates (denoted by δz_A and δz_B), we calculated the electric polarization in a point charge model, P_{ion} . For a more detailed discussion, we also estimated the Born effective charges

Table 2. Comparison of Polar Cation Displacements (δz_A and δz_B) and Calculated Electric Polarizations (P_{ion} and P_{BEC}) Among Various LiNbO_3 -Type ($R3c$) Compounds.^a

| Compound | δz_A | δz_B | $P_{\text{ion}} / \mu\text{C cm}^{-2}$ | $P_{\text{BEC}} / \mu\text{C cm}^{-2}$ |
|--------------------------------|--------------|--------------|--|--|
| InFeO_3 | 0.0506 | 0.0177 | 82 | 96 |
| ScFeO_3 ³⁹ | 0.0607 | 0.0212 | 100 | 107 |
| ZnTiO_3 ³⁷ | 0.0487 | 0.0196 | 75 | 88 |
| ZnSnO_3 ²⁸ | 0.0483 | 0.0124 | 59 | 65 |
| LiNbO_3 ⁷⁴ | 0.0487 | 0.0200 | 67 | 76 |

^aThe centrosymmetric $R\bar{3}c$ perovskite-type structure is used as the parent structure. δz_A and δz_B represent the displacements along the hexagonal c -axis of A - and B -site cations with respect to the surrounding oxide ions in the atomic coordinates, respectively (see Figure 3). P_{ion} is the polarization calculated by using the formal charges of ions and their relative displacements along the c -axis. P_{BEC} is the polarization calculated by using the Born effective charges (see section 2).

Table 3. Born Effective Charges Tensors, $Z^*_{\alpha\beta}$, in Cartesian Coordinates for Representative Five Atoms in $R\bar{3}c$ InFeO_3 .^a

| Atom | $Z^*_{\alpha\beta}$ | | |
|---------------|---------------------|-------|-------|
| In_1 | 3.54 | 0.00 | 0.00 |
| | 0.00 | 3.54 | 0.00 |
| | 0.00 | 0.00 | 3.51 |
| Fe_1 | 3.98 | -0.16 | 0.00 |
| | 0.16 | 3.98 | 0.00 |
| | 0.00 | 0.00 | 3.60 |
| O_1 | -2.21 | 0.00 | 0.00 |
| | 0.00 | -2.80 | -0.56 |
| | 0.00 | -0.61 | -2.37 |
| O_2 | -2.65 | -0.25 | 0.49 |
| | -0.25 | -2.36 | 0.28 |
| | 0.53 | 0.30 | -2.37 |
| O_3 | -2.65 | -0.25 | 0.49 |
| | -0.25 | -2.36 | 0.28 |
| | 0.53 | 0.30 | -2.37 |

^aIn Cartesian (x, y, z) coordinates, the z -axis is along the hexagonal c direction, the y -axis is in a gliding plane perpendicular to the a -axis, and x along a .

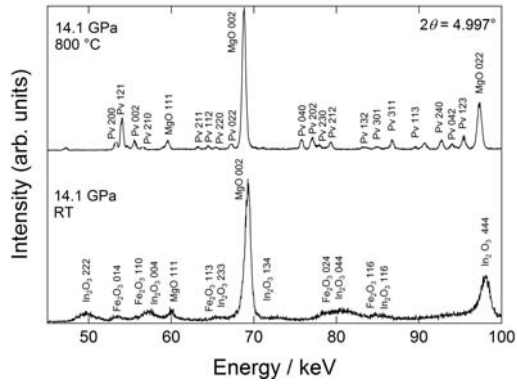


Figure 4. *In situ* SXR D patterns of InFeO₃ measured by the energy-dispersive method: a pressure of 14.1 GPa was applied to a mixture of In₂O₃ (bixbyte-type) and Fe₂O₃ (corundum-type) at room temperature (lower) and then the temperature was increased to 800 °C (upper). Pv denotes the orthorhombic perovskite. MgO is the pressure maker.

the solid-state reaction proceeds between In₂O₃ and Fe₂O₃ and leads to the formation of another crystalline phase. The diffraction pattern can be indexed in an orthorhombic perovskite-type structure with a space group of either *Pnma* or *Pn2₁a*. Although corundum-type InFeO₃ was obtained at 6 GPa and 850 °C,⁵⁷ our investigation demonstrates that applying higher pressures up to 15 GPa yields a new polymorph, orthorhombic perovskite-type InFeO₃. The orthorhombic perovskite is unquenchable to ambient condition but instead transforms into the polar *R3c* phase, LiNbO₃-type InFeO₃, as shown in section 3.1. Consequently, LiNbO₃-type InFeO₃ is not a high-pressure stable phase but a metastable quench product from the high-pressure phase. A similar phase transformation was observed in the formation process of LiNbO₃-type oxides such as MnTiO₃,²² MnSnO₃,²³ FeTiO₃,²⁴ and ScFeO₃.³⁹

So far, transition-metal perovskite oxides containing In³⁺ ions, such as InCrO₃,⁷⁹ In₂NiMnO₆,⁸⁰ and InRhO₃,⁸¹ have been synthesized by using high pressure and high temperature conditions. The structural refinements for these compounds revealed that In³⁺ ion has a strong preference for *A*-site occupation in the orthorhombic perovskite-type structure. This also should hold for the present case, i.e., orthorhombic perovskite InFeO₃, although its structural refinement was impossible to perform because of the poor data quality of energy-dispersive SXR D profiles. The phase transformation upon decompression occurs as a result of a change in the FeO₆ octahedral tilt pattern from $\bar{a}^-b^+a^-$ (in *Pnma* or *Pn2₁a*) to $\bar{a}^-a^-a^-$ (in *R3c*) and therefore does not necessarily involve the change in the cation distribution between the *A*- and *B*-sites. It is thus considered that the pressure-induced stabilization of the orthorhombic perovskite phase with In³⁺ and Fe³⁺ ions fully ordered on the *A*- and *B*-sites is a key step to synthesize LiNbO₃-type InFeO₃.

3.4 Magnetic Properties. Figure 5 shows ⁵⁷Fe Mössbauer spectra of LiNbO₃-type InFeO₃ at various temperatures. The spectrum at 4 K consists of a well-defined magnetic sextet, indicating the presence of long-range magnetic ordering. As the temperature is raised, the magnetic splitting decreases gradually and collapses into a paramagnetic doublet at 516 K. These spectra were analyzed by least-squares fitting using the Lorentzian function. The obtained Mössbauer parameters at 4 K, room temperature, and 516 K are summarized in Table 3. The isomer shift (IS = 0.36 mm s⁻¹) and hyperfine field (HF = 460 kOe) at room temperature are indicative of the high-spin state (*S* = 5/2) of Fe³⁺ ion. The quadrupole interaction estimated from the magnetically split spectra, which is equal to *S*₁ – *S*₂ in Figure 5,

almost temperature independent (e.g., 0.36 mm s⁻¹ at room temperature), and is very close to the quadrupole splitting in the paramagnetic state at 516 K (QS = 0.40 mm s⁻¹), suggesting the alignment of Fe³⁺ spins perpendicular to the hexagonal *c*-axis, corresponding to the principal axis of the electric field gradient.⁸² We also find that the absolute value of QS is nearly an order of magnitude larger than those of orthorhombic perovskites RFeO₃ (*R* = La–Lu and Y) with nearly regular FeO₆ octahedra (typically below 0.02 mm s⁻¹).⁸³ This result means that the oxygen octahedral coordination for Fe³⁺ ions in LiNbO₃-type InFeO₃ is highly asymmetric with a large electric field gradient, consistent with the aforementioned structural data showing the strong off-centering distortion of FeO₆ octahedra.

Temperature evolution of TOF NPD patterns measured on WISH is displayed in Figure 6a. For the paramagnetic state at 600 K, all the diffraction peaks are ascribed to the nuclear reflections (see also Figure 1b). As the temperature is lowered, additional peaks appear at *d* = 4.66 Å and 4.34 Å and grow in intensity. This observation, together with the result of variable-temperature Mössbauer spectra, indicates that the two peaks are of magnetic origin. These magnetic reflections are

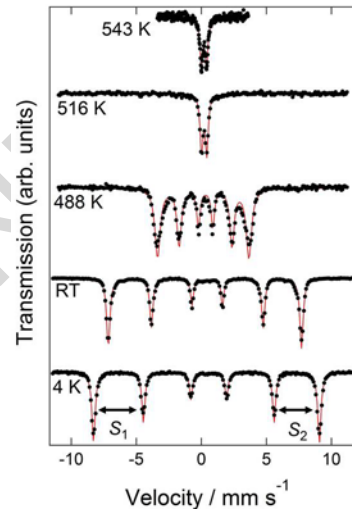


Figure 5. ⁵⁷Fe Mössbauer spectra of LiNbO₃-type InFeO₃ at various temperatures. The dots represent the experimental data, and the solid red lines the total fits. *S*₁ and *S*₂ denote the relative shifts of the peaks.

Table 4. Hyperfine Parameters (IS, QS, and HF) of ⁵⁷Fe Mössbauer Spectra for LiNbO₃-type InFeO₃.^a

| Temperature | IS (mm s ⁻¹) | QS (mm s ⁻¹) | HF (kOe) |
|-------------|--------------------------|--------------------------|----------|
| 4 K | 0.48 | 0.36 ^b | 540 |
| RT | 0.36 | 0.36 ^b | 460 |
| 516 K | 0.22 | 0.40 | 0 |

^aIS, QS, and HF denote the isomer shift, quadrupole splitting, and hyperfine field, respectively. ^bQS at 4 K and room temperature is defined as a difference of *S*₁ and *S*₂, *S*₁ – *S*₂, as shown in Figure 5.

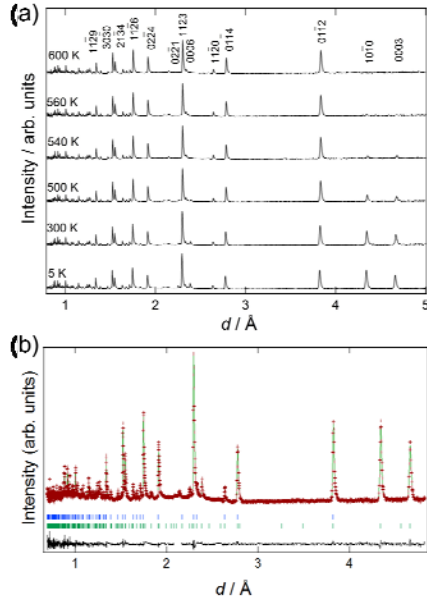


Figure 6. (a) Temperature evolution of TOF NPD (bank 2 data, $2\theta = 121.68^\circ$) for LiNbO₃-type InFeO₃, showing the magnetic reflections 0003 and $10\bar{1}1$. (b) Rietveld refinement of TOF NPD data at 5 K, showing the observed (red crosses) and calculated (green solid line) profiles and the difference between the observed and calculated profiles (black solid line). A vanadium peak at $d \sim 2.15$ Å originating from the sample holder is excluded in the refinement. The upper and lower ticks correspond to the positions of the calculated nuclear and magnetic Bragg reflections for $R3c$ InFeO₃, respectively.

indexed as 0003 and $10\bar{1}1$, respectively, with a propagation vector $\mathbf{k} = 0$; that is, the magnetic cell is equivalent to the chemical cell. Representation analysis on the $R3c$ space group with Jana2006⁸⁴ shows that the magnetic representation decomposes into three one-dimensional irreducible representations (irreps) as $\Gamma = \Gamma_1 + \Gamma_2 + 4\Gamma_3$. The irreps Γ_1 and Γ_2 represent antiferromagnetic and ferromagnetic spin orders along the c -axis, respectively, and these models fail to reproduce the emergence of two magnetic reflections. The irrep Γ_3 is composed of four basis vectors that dictate antiferromagnetic and ferromagnetic spin orders in the ab -plane. Upon comparing the different solutions, a good fit of the experimental data is obtained with a combination of Γ_3 basis vectors (see Figure 6b), which describes a G-type antiferromagnetic ordering with the Fe³⁺ moments lying in the ab -plane, as shown in Figure 7a. The magnetic structure is consistent with the Mössbauer analysis showing the Fe³⁺ spins oriented in directions perpendicular to the c -axis. The TOF NPD data for $5 \leq T \leq 540$ K can be reasonably refined by using the magnetic structure depicted in Figure 7a. Successful refinements are also confirmed for the NPD data recorded at WOMBAT (Figures S3 and S4 and Table S2). The refined magnetic moment at 5 K is $\mu = 3.95(3) \mu_B / \text{Fe}$ from the WISH data and $\mu = 3.92(8) \mu_B / \text{Fe}$ from the WOMBAT data. These values are lower than the ideal value of $5 \mu_B$ expected for high-spin ($S = 5/2$) Fe³⁺ ions.

Using the spin-orbit coupling implementation of DFT, we estimated the magnetocrystalline anisotropy energy for the G-type antiferromagnetic structure optimized at 5 K. One can see from Figure 7b that the hard magnetic direction is along the c -axis and an easy direction of magnetization is in the ab -plane. In other words, the Fe³⁺ moments are expected to align perpendicular to the c -axis, which agrees with the experimental description of the magnetic structure. Thus, the smaller-than-expected magnetic moment may be related to the spin-orbit coupling, and this should

cause the antisymmetric exchange for certain low symmetries, so-called DM interaction.^{50,51}

Given the absence of inversion center between nearest-neighboring Fe³⁺ ions, the symmetry allows a canting of antiferromagnetically ordered Fe³⁺ spins through the DM exchange, resulting in a macroscopic magnetization, i.e., weak ferromagnetism. Figure 8 shows the magnetic field dependence of magnetization at 5 and 300 K. Weakly ferromagnetic signals are clearly observed in the antiferromagnetically ordered state ($T \leq 540$ K). The saturation moment of the ferromagnetic component at 5 K is $\sim 0.03 \mu_B / \text{Fe}$, indicating a canting angle of $\sim 0.2^\circ$ of antiferromagnetically ordered Fe³⁺ ($S = 5/2$) spins. The presence of such a small spin canting is far below the detection limits of the NPD technique; indeed, no significant improvement to the fit was found by considering the spin canting.

4. DISCUSSION

4.1 Magnetic Transition. Magnetic characterization for LiNbO₃-type ($R3c$) InFeO₃ (section 3.4) reveals a weak ferromagnetic (canted antiferromagnetic)–paramagnetic transition well above room temperature. We examined the critical behavior of the magnetic transition using the temperature-dependent magnetic moments derived from NPD data, the result of which is Figure 9. It is found that the temperature dependence of magnetic moments derived from WISH and WOMBAT data is almost the same as each other. The temperature dependence of magnetic moment in the vicinity of the Néel temperature, T_N , is expressed as $\mu(T) = \mu(0) (1 - T/T_N)^\beta$, where $\mu(0)$ is the magnetic moment at 0 K, and β is the critical exponent. Here, we adopt the WOMBAT data because of the presence of more data points around T_N . The fitting to the experimental data between 400 and

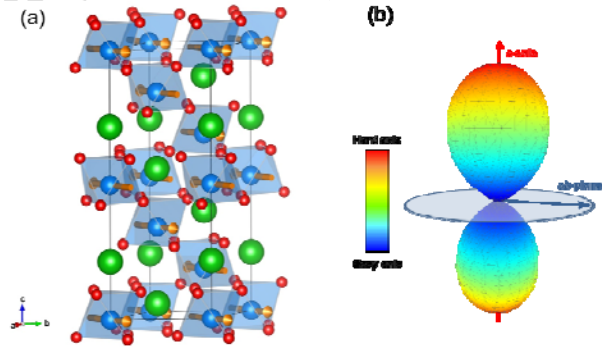


Figure 7. (a) Magnetic structure of LiNbO₃-type InFeO₃. Green, blue, and red spheres represent In, Fe, and O atoms, respectively, highlighting the three-dimensional network of corner-sharing FeO₆ octahedra. Orange arrows denote the direction of the magnetic moment of Fe³⁺. (b) Magnetocrystalline anisotropy energy calculated for G-type antiferromagnetic LiNbO₃-type InFeO₃. The three-dimensional shape shows that the easy direction of magnetization is in the ab -plane.

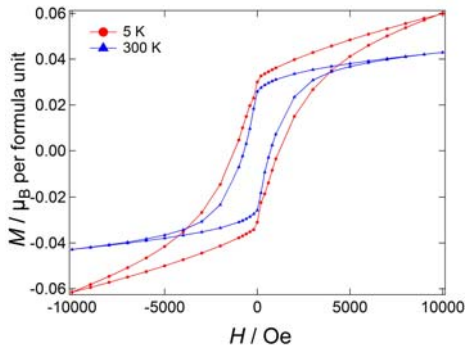


Figure 8. Magnetic field dependence of the magnetization of LiNbO₃-type InFeO₃ at 5 and 300 K.

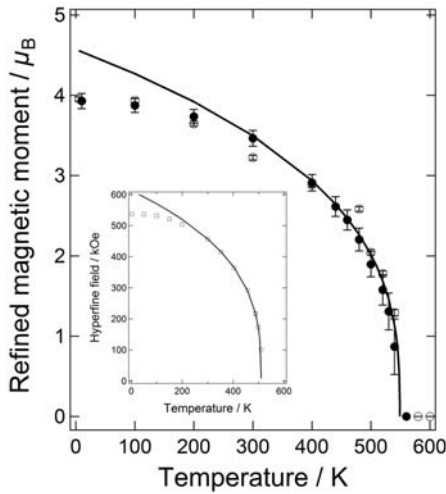


Figure 9. Temperature dependence of the magnetic moment of LiNbO₃-type InFeO₃ refined by TOF NPD at WISH (open circles) and NPD at WOMBAT (solid circles). The solid curve represents the critical law fitting to WOMBAT data. The inset shows the temperature dependence of hyperfine field (open squares) and the critical law fitting (solid line).

540 K gives $\mu(0) = 4.6(2)\mu_B$, $T_N = 545(1)$ K, and $\beta = 0.346(3)$. The critical exponent is close to the theoretical value for a three-dimensional XY magnet ($\beta = 0.34$), consistent with the magnetic structure where Fe³⁺ spins lie in the *ab*-plane (see Figure 7). We also performed the power-law fitting to temperature-dependent Mössbauer hyperfine fields between 400 and 500 K (see the inset of Figure 9). The estimated Néel temperature of $T_N = 510.1(1.2)$ K is only slightly lower than that determined by NPD, and the critical exponent of $\beta = 0.329(12)$ is almost the same as that derived from the NPD investigation. Such critical behavior has been also found in the vicinity of T_N for R3c MnTiO₃ ($\beta = 0.38$),⁸⁵ R3c BiFeO₃ ($\beta = 0.37$),⁸⁶ and Pnma RFeO₃ ($R = \text{La-Lu}$, and Y, $\beta = 0.34-0.36$).⁸³

Since both LiNbO₃-type AFeO₃ ($A = \text{In}$ and Sc) and orthorhombic perovskites RFeO₃ ($R = \text{La-Lu}$, and Y) have a corner-shared FeO₆ network, it is interesting to investigate the relation between the Fe–O–Fe bond angle, α , and the magnetic transition temperature, T_N . The value of T_N for InFeO₃ is comparable to that for ScFeO₃ ($T_N = 545$ K),³⁹ but is lower than those for RFeO₃ ($T_N = 740-623$ K).⁸³ Given the smaller Fe–O–Fe bond angles in InFeO₃ ($\alpha = 139^\circ$) and ScFeO₃ ($\alpha = 135^\circ$)³⁹ in comparison with RFeO₃ ($\alpha = 157-141^\circ$),^{53,54} the reduction in T_N for InFeO₃ and ScFeO₃ is ascribable to weakened superexchange interactions. Here, it is worth emphasizing that

InFeO₃ and ScFeO₃ still have magnetic transition temperatures much higher than room temperature, although other known LiNbO₃-type magnets have been reported to exhibit the magnetic ordering below room temperature; e.g., $T_N = 110$ K for FeTiO₃,²⁹ $T_N = 24$ K for MnTiO₃,^{32,85} and $T_N = 22$ K for Zn₂FeTaO₆.³⁸ Recently, Belik *et al.*³⁰ reported the magnetic transition temperature close to room temperature ($T_N = 270$ K) for LiNbO₃-type (In_{1-x}M_x)MO₃ ($x \approx 0.111-0.176$; $M = \text{Fe}_{0.5}\text{Mn}_{0.5}$). The M –O– M bond angle, $\alpha = 138^\circ$, is not so different from those for InFeO₃ and ScFeO₃, but the presence of equal amounts of Mn³⁺ and Fe³⁺ ions on the *B*-sites makes the Mn³⁺ ($S = 2$)–O–Fe³⁺ ($S = 5/2$) superexchange interaction dominant, rather than the Fe³⁺ ($S = 5/2$)–O–Fe³⁺ ($S = 5/2$) superexchange one, which significantly lowers the magnetic transition temperature compared to ScFeO₃ and InFeO₃. This highlights the importance of the full occupancy of the *B*-site by Fe³⁺ ions to achieve above-room-temperature magnetic ordering.

4.2 Role of *A*-site Cation in Stabilizing Polar Structural Distortions. As described in section 3.2, a sizable electric polarization of 96 $\mu\text{C}/\text{cm}^2$ is predicted for R3c InFeO₃. Remarkably, the polarization value is comparable to that of an isostructural and SOJT-active perovskite ferroelectric, R3c BiFeO₃ (90-100 $\mu\text{C}/\text{cm}^2$).^{77,78,87} Thus, it is of great interest to compare the role of the *A*-site cation in stabilizing the polar structural distortion between BiFeO₃ and InFeO₃. In BiFeO₃, the orbital overlap between Bi 6s and O 2p states results in a set of bonding and antibonding states, both of which are filled. The occupied antibonding levels are stabilized by the mixing further with Bi 6p states, which lie in the conduction band. For *s* and *p* states of different parity, the *sp* mixing is allowed if the cation site does not possess inversion symmetry.⁸⁸ The overlap between the Bi 6s/6p and O 2p orbitals results in the stereochemical activity of the Bi³⁺ lone pair and induces an SOJT distortion to the polar R3c.⁷⁵ The role of the charge transfer through cation-anion orbital overlap manifests itself in the Born effective charges, which can be interpreted as the amount of charge that effectively contributes to the polarization during the displacement of a given ion,⁸⁹ or the change in covalency with respect to the displacement of a given ion. The redistribution of the electrons between covalently bonded cation–anion pairs upon ionic displacements leads to anomalously larger Born effective charges in magnitude relative to their formal charges. For BiFeO₃, the Born effective charge of Bi cation ($Z_{\text{Bi}}^* = +4.92$) is much larger than its formal charge (+3), leading to a larger polarization than would arise from the ionic component alone.^{77,78}

In the case of InFeO₃, however, the lone-pair-driven mechanism cannot be expected because the *A*-site In³⁺ ion has a fully filled 4d electronic structure, 4d¹⁰. Indeed, a very small contribution of the charge transfer in In–O bonds manifests itself in the Born effective charges close to their formal charges as seen in Table 3. Similarly, the orbital overlap in Fe–O bonds, while it plays a role in the spin-orbit coupling, is not indicative of anomalies in the Born effective charges (see Table 3). As a result, the large polarization in InFeO₃ evolves in such a way as to stabilize electrostatically the coordination environments about both the *A*- and *B*-sites, unlike in BiFeO₃. This is also applicable to a recently developed Sc analog, R3c ScFeO₃.³⁹ Although the *A*-site Sc³⁺ ion does not possess a lone pair of electrons, a large electric polarization of $P_{\text{BEC}} = 107$ $\mu\text{C}/\text{cm}^2$ is predicted. No significant anomalies are found in the Born effective charges; $Z_{\text{Sc}}^* = 3.35$ and $Z_{\text{Fe}}^* = 3.37$, and $Z_{\text{O}}^* = -2.22$. The occurrence of the large polarizations in the two compounds containing no lone-pair *A*-site cations confirms a common mechanism underlying the structural distortions to R3c.

Recent first-principle calculations in combination with symmetry arguments have shown that most of

small-tolerance-factor $R\bar{3}c$ perovskite oxides (i.e., LiNbO_3 -type oxides) belong to a family of A -site driven geometric ferroelectrics where the A -site cation displacements from the centrosymmetric $R\bar{3}c$ to the polar $R3c$ arise entirely from the electrostatic interactions.¹² The A -site cations are nine-coordinated in $R\bar{3}c$, with three short in-plane oxide ions and six long out-of-plane oxide ions (see Figure 3). When $R\bar{3}c$ has a noticeable magnitude of the $a^-a^-a^-$ octahedral tilts, the A -site cations become electrostatically unstable because they are too far from the out-of-plane oxide ions; namely, the A -O bonds are virtually confined to the three in-plane oxide ions, meaning that the A -site is underbonded. This instability drives the A -site cations to move toward three of the six out-of-plane oxide ions in order to form InO_6 octahedra, which gives rise to the polar distortion to $R3c$. In addition to the A -site cation size (i.e., tolerance factor t), the A -site cation valence will have an impact on the relative stability of $R\bar{3}c$ and $R3c$ through the A -O Coulomb interactions. As argued by Xiang,⁹⁰ when the higher valence cations are incorporated in the A -site, $R\bar{3}c$ is even more unstable against $R3c$ because of the increased Coulomb interaction. This may explain why the trivalent A -site cations in InFeO_3 and ScFeO_3 undergo the larger polar displacements compared to the divalent or monovalent A -site cations in other compounds such as ZnTiO_3 , ZnSnO_3 , and LiNbO_3 (see Table 2). The A -site cation displacements are inevitably accompanied by the off-centering BO_6 distortion through an electrostatic Coulomb repulsion between cations in the face-sharing octahedra stacked along the hexagonal c -axis (see also Figure 2b). Interestingly, the off-centering distortion for $d^5 \text{Fe}^{3+}$ ions in InFeO_3 ($\Delta = 14.7 \times 10^{-4}$) is only slightly smaller than those for SOJT-active d^0 cations in ZnTiO_3 ($\Delta = 47 \times 10^{-4}$ for TiO_6)³⁷ and LiNbO_3 ($\Delta = 40 \times 10^{-4}$ for NbO_6).^{72,74} This is ascribed to the relatively large cation-cation repulsion across the shared octahedral face for A^{3+} - B^{3+} pairs as compared to A^{2+} - B^{4+} or A^+ - B^{5+} pairs.

4.3 Potential of Magnetoelectric Coupling Having demonstrated the coexistence of polar structural distortion and weak ferromagnetism at room temperature for $R3c \text{InFeO}_3$, it is worthwhile to comment on its potential as a magnetoelectric multiferroic, especially its ability to control the magnetism with an electric field. The electric-field control of weak ferromagnetism has been a focus of research in multiferroics.^{52,91-93} As mentioned in section 3.4, the weak ferromagnetism in $R3c \text{InFeO}_3$ results from a slight canting of the Fe^{3+} moments in a G-type antiferromagnetic arrangement as a consequence of a spin-orbit effect on the superexchange interaction, i.e., the DM exchange interaction. Such an interpretation of the experimental data is corroborated by DFT calculations with spin-orbit coupling included. Let us consider an orthonormal frame (x , y , z) with z -axis defined as the hexagonal c direction (or pseudocubic [111] direction). Our DFT calculations start from a collinear antiferromagnetic order with the magnetic moments aligned along the x -axis. The spin-orbit inclusion leads to a weak ferromagnetic moment of $0.02 \mu_B / \text{Fe}$ along the y -axis with an electric polarization being $\sim 90 \mu\text{C}/\text{cm}^2$ along the z -axis. The magnitude of the canted magnetic moment is in good agreement with the experimental observation (see Figure 8). A similar situation has been reported for $R3c \text{BiFeO}_3$ where the DM interaction is responsible for the canted Fe^{3+} moments in an otherwise G-type antiferromagnetic structure.⁹¹ For BiFeO_3 , the inversion symmetry, the center of which is at the midpoint between nearest-neighboring Fe^{3+} ions, is broken by the antiferrodistortive FeO_6 octahedral tilts (rather than the polar structural distortion), which yields the nonzero DM interaction.⁹¹ The same should hold true for InFeO_3 in terms of symmetry considerations. The occurrence of weak ferromagnetism in InFeO_3 , unlike the cycloidal magnetic

modulation in BiFeO_3 (in the bulk), is presumably associated with a larger magnitude of the FeO_6 octahedral tilts in InFeO_3 ($\varphi = 27.3^\circ$) with respect to BiFeO_3 ($\varphi = 13.8^\circ$).⁴⁶ This also account for why $R3c \text{ScFeO}_3$ with a highly tilted octahedral network ($\varphi \sim 30^\circ$) exhibits a canted G-type antiferromagnetsim.³⁹

Although a linear magnetoelectric coupling is symmetry-allowed in $R3c \text{InFeO}_3$, direct 180° switching of the weak ferromagnetism by the electric polarization is unlikely to occur, as argued for $R3c \text{BiFeO}_3$ (in the case that the weak ferromagnetism appears due to the suppression of the cycloidal magnetic modulation).⁹¹ This is because such control of magnetoelectric domains requires the FeO_6 octahedral tilts to change the sense, which is kinetically too demanding when based on a one-step switching path. In contrast, it has been recently evidenced, from both theory and experiments, that the magnetization reversal can be achieved based on a two-step kinetic path,^{92,93} in BiFeO_3 , for example, the FeO_6 octahedral tilts follow a sequential rotation of the polarization direction (71° and 109° switching events) upon application of an electric field and thus lead to the reversal of weak ferromagnetism.⁹² Considering the nontrivial role which the DM interaction plays for the two-step domain switching, the electric-field-induced magnetization reversal is expected to be possible in $R3c \text{InFeO}_3$ and also in $R3c \text{ScFeO}_3$.

5. SUMMARY

We have found two new polymorphs of InFeO_3 , orthorhombic perovskite-type and LiNbO_3 -type InFeO_3 ; the former orthorhombic phase ($Pnma$ or $Pn2_1a$) is stabilized under pressures up to 15 GPa and high temperatures above 1000 °C and transformed into the latter rhombohedral $R3c$ phase upon decompression. The polar structural distortion in $R3c$ consists of a large displacement of A -site In^{3+} (d^{10}) ions and a small off-centering displacement of B -site Fe^{3+} (d^5) ions within oxygen octahedra. A minor role of SOJT distortions in stabilizing the polar structure is confirmed by a lack of any significant anomalies in the Born effective charges. These results are in sharp contrast to the case of an isostructural perovskite ferroelectric, $R3c \text{BiFeO}_3$, where the large polar displacement of $6s^2 \text{Bi}^{3+}$ ions is driven by the SOJT effect forming lone-pair electrons and thus displays an anomaly in the effective charge. Even though there is little contribution of SOJT distortion, the theoretical electric polarization of LiNbO_3 -type InFeO_3 is as large as $96 \mu\text{C}/\text{cm}^2$, which is comparable to that of BiFeO_3 (90 – $100 \mu\text{C}/\text{cm}^2$). For $R3c \text{InFeO}_3$, we also observe long-range magnetic ordering of the Fe^{3+} sublattice well above room temperature ($T_N \sim 545 \text{ K}$) due to the strong Fe-O-Fe superexchange interaction. The lack of an inversion symmetry in the superexchange pathway gives rise to the nonzero DM interaction, leading to the weak ferromagnetism due to a slight canting of the Fe^{3+} moments in an otherwise G-type antiferromagnetic arrangement; the ferromagnetic component is perpendicular to the direction of the electric polarization resulting from the cation displacements. Our results thus demonstrate that $R3c \text{InFeO}_3$ is a typical geometric polar material and possesses both a spontaneous magnetization and a polar structural distortion at room temperature and higher. These findings provide chemical and structural selection guidelines to aid in the search for “room-temperature” polar magnets.

ASSOCIATED CONTENT Supporting Information.

Crystallographic data (CIF format), additional data of sample characterization, and a calculation method using the spin-orbit

coupling implementation of DFT. This material is available free of charge via the Internet at <http://pubs.acs.org>.

AUTHOR INFORMATION

Corresponding Author

*fujita@dipole7.kuic.kyoto-u.ac.jp

Present Addresses

†Laboratory for Materials and Structures, Institute of Innovative Research, Tokyo Institute of Technology, Yokohama 226-8503, Japan

Author Contributions

The manuscript was written through contributions of all authors. All authors have given approval to the final version of the manuscript.

Notes

The authors declare no competing financial interest.

ACKNOWLEDGMENT

The authors thank I. Tanaka of Kyoto University for the first-principles calculations and C. Tassel of Kyoto University for useful comments in NPD analysis. NPD experiments at WISH and WOMBAT were supported by beam time allocation from STFC (RB1410149) and ANSTO (P3177), respectively. Travel costs of K.F. and T.K. for the experiments at WOMBAT were partly supported by Institute for Solid State Physics, The University of Tokyo (Proposal No. 12693), JAEA. The SXR D at ambient pressure and *in-situ* energy-dispersive SXR D experiments under high-pressure conditions were performed at the BL02B2 (Proposal Nos. 2013B1742, 2014A1683, and 2014B1726) and BL04B1 (Proposal No. 2013B1662) beamlines of SPring-8, respectively, with the approval of JASRI. This work was partly supported by JSPS KAKENHI Grant-in-Aids for Scientific Research (A) (Grant Nos. 25249090 and 25248016), Scientific Research on Innovative Areas “Nano Informatics” (Grant No. 26106514), and JSPS Fellows (Grant No. 15J08052).

REFERENCES

- (1) Catalan, G.; Scott, J. F. Physics and Applications of Bismuth Ferrite. *Adv. Mater.* **2009**, *21*, 2463–2485.
- (2) Smolenskii, G. A.; Chupis, I. E. Ferroelectromagnets. *Sov. Phys. Usp.* **1982**, *25*, 475–493.
- (3) Kiselev, S. V.; Ozerov, R. P.; Zhdanov, G. S. Detection of Magnetic Order in Ferroelectric BiFeO₃ by Neutron Diffraction. *Sov. Phys. Dokl.* **1963**, *7*, 742–744.
- (4) Sosnowska, I.; Peterlin-Neumaier, T.; Steichele, E. Spiral Magnetic Ordering in Bismuth Ferrite. *J. Phys. C: Solid State Phys.* **1982**, *15*, 4835–4846.
- (5) Smith, R. T.; Achenbach, G. D.; Gerson, R.; James, W. J. Dielectric Properties of Solid Solutions of BiFeO₃ with Pb(Ti,Zr)O₃ at High Temperature and High Frequency. *J. Appl. Phys.* **1968**, *39*, 70–74.
- (6) Teague, J. R.; Gerson, R.; James, W. J. Dielectric Hysteresis in Single Crystal BiFeO₃. *Solid State Commun.* **1970**, *8*, 1073–1074.
- (7) Palkar, V. R.; Kundaliya, D. C.; Malik, S. K.; Bhattacharya, S. Magnetoelectricity at Room Temperature in the Bi_{0.9-x}Tb_xLa_{0.1}FeO₃ System. *Phys. Rev. B* **2004**, *69*, 212102.
- (8) Kubota, M.; Oka, K.; Yabuta, H.; Miura, K.; Azuma, M. Structure and Magnetic Properties of BiFe_{1-x}Co_xO₃ and Bi_{0.9}Sm_{0.1}Fe_{1-x}Co_xO₃. *Inorg. Chem.* **2013**, *52*, 10698–10704.
- (9) Wang, J.; Neaton, J. B.; Zheng, H.; Nagarajan, V.; Ogale, S. B.; Liu, B.; Viehland, D.; Vaithyanathan, V.; Schlom, D. G.; Waghmare, U. V.; Spaldin, N. A.; Rabe, K. M.; Wuttig, M.; Ramesh, R. Epitaxial BiFeO₃ Multiferroic Thin Film Heterostructures. *Science* **2003**, *299*, 1719–1722.

- (10) Sando, D.; Agbelele, A.; Rahmedov, D.; Liu, J.; Rovillain, P.; Toulouse, C.; Infante, I. C.; Pyatakov, A. P.; Fusil, S.; Jacquet, E.; Carrétero, C.; Deranlot, C.; Lisenkov, S.; Wang, D.; Breton, J.-M. L.; Cazayous, M.; Sacuto, A.; Juraszek, J.; Zvezdin, A. K.; Bellaiche, L.; Dkhil, B.; Barthélémy, A.; Bibes, M. Crafting the Magnonic and Spintronic Response of BiFeO₃ Films by Epitaxial Strain. *Nat. Mater.* **2013**, *12*, 641–646.
- (11) Bai, F.; Wang, J.; Wuttig, M.; Li, J.; Wang, N.; Pyatakov, A. P.; Zvezdin, A. K.; Cross, L. E.; Viehland, D. Destruction of Spin Cycloid in (111)_c-oriented BiFeO₃ Thin Films by Epitaxial Constraint: Enhanced Polarization and Release of Latent Magnetization. *Appl. Phys. Lett.* **2005**, *86*, 032511.
- (12) Benedek, N. A.; Fennie, C. J. Why Are There So Few Perovskite Ferroelectrics? *J. Phys. Chem. C* **2013**, *117*, 13339–13349.
- (13) Kimura, T.; Goto, T.; Shintani, H.; Ishizaka, K.; Arima, T.; Tokura, Y. Magnetic Control of Ferroelectric Polarization. *Nature* **2003**, *426*, 55–58.
- (14) Tokunaga, Y.; Taguchi, Y.; Arima, T.; Tokura, Y. Electric-Field-Induced Generation and Reversal of Ferromagnetic Moment in Ferrites. *Nat. Phys.* **2012**, *8*, 838–844.
- (15) Van Den Brink, J.; Khomskii, D. I. Multiferroicity due to Charge Ordering. *J. Phys. Condens. Matter* **2008**, *20*, 434217.
- (16) Van Aken, B. B.; Palstra, T. T. M.; Filippetti, A.; Spaldin, N. A. The Origin of Ferroelectricity in Magnetoelectric YMnO₃. *Nat. Mater.* **2004**, *3*, 164–170.
- (17) Pitcher, M. J.; Mandal, P.; Dyer, M. S.; Alaria, J.; Borisov, P.; Niu, H.; Claridge, J. B.; Rosseinsky, M. J. Tilt Engineering of Spontaneous Polarization and Magnetization Above 300 K in a Bulk Layered Perovskite. *Science* **2015**, *347*, 420–424.
- (18) Syono, Y.; Akimoto, S.; Ishikawa, Y.; Endoh, Y. A New High Pressure Phase of MnTiO₃ and Its Magnetic Property. *J. Phys. Chem. Solids* **1969**, *30*, 1665–1672.
- (19) Syono, Y.; Sawamoto, H.; Akimoto, S. Disordered Ilmenite MnSnO₃ and Its Magnetic Property. *Solid State Commun.* **1969**, *7*, 713–716.
- (20) Ito, E.; Matsui, Y. High-Pressure Transformation in Silicates, Germanates, and Titanates with ABO₃ Stoichiometry. *Phys. Chem. Miner.* **1979**, *4*, 265–274.
- (21) Ko, J.; Prewitt, C. High-Pressure Phase Transition in MnTiO₃ from the Ilmenite to the LiNbO₃ Structure. *Phys. Chem. Miner.* **1988**, *15*, 355–362.
- (22) Ross, N. L.; Ko, J.; Prewitt, C. T. A New Phase Transition in MnTiO₃: LiNbO₃-Perovskite Structure. *Phys. Chem. Miner.* **1989**, *16*, 621–629.
- (23) Leinenweber, K.; Utsumi, W.; Tsuchida, Y.; Yagi, T.; Kurita, K. Unquenchable High-Pressure Polymorphs of MnSnO₃ and FeTiO₃. *Phys. Chem. Miner.* **1991**, *18*, 244–250.
- (24) Mehta, A.; Leinenweber, K.; Navrotsky, A.; Akaogi, M. Calorimetric Study of High Pressure Polymorphism in FeTiO₃: Stability of the Perovskite Phase. *Phys. Chem. Miner.* **1994**, *21*, 207–212.
- (25) Leinenweber, K.; Linton, J.; Navrotsky, A.; Fei, Y.; Parise, J. B. High-Pressure Perovskites on the Join CaTiO₃-FeTiO₃. *Phys. Chem. Miner.* **1995**, *22*, 251–258.
- (26) Linton, J. A.; Fei, Y.; Navrotsky, A. Complete Fe-Mg Solid Solution in Lithium Niobate and Perovskite Structures in Titanates at High Pressures and Temperatures. *Am. Mineral.* **1997**, *82*, 639–642.
- (27) Navrotsky, A. Energetics and Crystal Chemical Systematics among Ilmenite, Lithium Niobate, and Perovskite Structures. *Chem. Mater.* **1998**, *10*, 2787–2793.
- (28) Inaguma, Y.; Yoshida, M.; Katsumata, T. A Polar Oxide ZnSnO₃ with a LiNbO₃-Type Structure. *J. Am. Chem. Soc.* **2008**, *130*, 6704–6705.
- (29) Varga, T.; Kumar, A.; Vlahos, E.; Denev, S.; Park, M.; Hong, S.; Sanhira, T.; Wang, Y.; Fennie, C. J.; Streiffer, S. K.; Ke, X.; Schiffer, P.; Gopalan, V.; Mitchell, J. F. Coexistence of Weak Ferromagnetism and Ferroelectricity in the High Pressure LiNbO₃-Type Phase of FeTiO₃. *Phys. Rev. Lett.* **2009**, *103*, 047601.
- (30) Belik, A. A.; Furubayashi, T.; Matsushita, Y.; Tanaka, M.; Hishita, S.; Takayama-Muromachi, E. Indium-Based Perovskites: A New Class of Near-Room-Temperature Multiferroics. *Angew. Chem. Int. Ed.* **2009**, *48*, 6117–6120.
- (31) Inaguma, Y.; Tanka, K.; Tsuchiya, T.; Mori, D.; Katsumata, T.; Ohba, T.; Hiraki, K.; Takahashi, T.; Saitoh, H. Synthesis, Structural Transformation, Thermal Stability, Valence State, and Magnetic and Electronic Properties of PbNiO₃ with Perovskite- and LiNbO₃-Type Structures. *J. Am. Chem. Soc.* **2011**, *133*, 16920–16929.
- (32) Aimi, A.; Katsumata, T.; Mori, D.; Fu, D. S.; Itoh, M.; Kyomen, T.; Hiraki, K.; Takahashi, T.; Inaguma, Y. High-Pressure Synthesis and

- Correlation between Structure, Magnetic, and Dielectric Properties in LiNbO₃-Type MnMO₃ (M = Ti, Sn). *Inorg. Chem.* **2011**, *50*, 6392–6398.
- (33) Belik, A. A.; Furubayashi, T.; Yusa, H.; Takayama-Muromachi, E. Perovskite, LiNbO₃, Corundum, and Hexagonal Polymorphs of (In_{1-x}M_x)MO₃. *J. Am. Chem. Soc.* **2011**, *133*, 9405–9412.
- (34) Arielly, R.; Xu, W. M.; Greenberg, E.; Rozenberg, G. Kh.; Pasternak, M. P.; Garbarino, G.; Clark, S.; Jeanloz, R. Intriguing Sequence of GaFeO₃ Structures and Electronic States to 70 GPa. *Phys. Rev. B* **2011**, *84*, 094109.
- (35) Li, M.-R.; Walker, D.; Retuerto, M.; Sarkar, T.; Hadermann, J.; Stephens, P. W.; Croft, M.; Ignatov, A.; Grams, C. P.; Hemberger, J.; Nowik, I.; Halasyamani, P. S.; Tran, T. T.; Mukherjee, S.; Dasgupta, T. S.; Greenblatt, M. Polar and Magnetic Mn₂FeMO₆ (M = Nb, Ta) with LiNbO₃-type Structure: High-Pressure Synthesis. *Angew. Chem. Int. Ed.* **2013**, *52*, 8406–8410.
- (36) Shi, Y.; Guo, Y.; Wang, X.; Princep, A. J.; Khalyavin, D.; Manuel, P.; Michiue, Y.; Sato, A.; Tsuda, K.; Yu, S.; Arai, M.; Shirako, Y.; Akaogi, M.; Wang, N.; Yamaura, K.; Boothroyd, A. T. *Nat. Mater.* **2013**, *12*, 1024–1027.
- (37) Inaguma, Y.; Aimi, A.; Shirako, Y.; Sakurai, D.; Mori, D.; Kojitani, H.; Akaogi, M.; Nakayama, M. High-Pressure Synthesis, Crystal Structure, and Phase Stability Relations of a LiNbO₃-Type Polar Titanate ZnTiO₃ and Its Reinforced Polarity by the Second-Order Jahn–Teller Effect. *J. Am. Chem. Soc.* **2014**, *136*, 2748–2756.
- (38) Li, M.-R.; Stephens, P. W.; Retuerto, M.; Sarkar, T.; Grams, C. P.; Hemberger, J.; Croft, M. C.; Walker, D.; Greenblatt, M. Designing Polar and Magnetic Oxides: Zn₂FeTaO₆ - in Search of Multiferroics. *J. Am. Chem. Soc.* **2014**, *136*, 8508–8511.
- (39) Kawamoto, T.; Fujita, K.; Yamada, I.; Matoba, T.; Kim, S. J.; Gao, P.; Pan, X.; Findlay, S. D.; Tassel, C.; Kageyama, H.; Studer, A. J.; Hester, J.; Irifune, T.; Akamatsu, H.; Tanaka, K. Room-Temperature Polar Ferromagnet ScFeO₃ Transformed from a High-Pressure Orthorhombic Perovskite Phase. *J. Am. Chem. Soc.* **2014**, *136*, 15291–15299.
- (40) Tassel, C.; Kuno, Y.; Goto, Y.; Yamamoto, T.; Brown, C. M.; Hester, J.; Fujita, K.; Higashi, M.; Abe, R.; Tanaka, K.; Kobayashi, Y.; Kageyama, H. MnTaO₂N: Polar LiNbO₃-type Oxynterite with a Helical Spin Order. *Angew. Chem. Int. Ed.* **2015**, *54*, 516–521.
- (41) Yu, R.; Hojo, H.; Mizoguchi, T.; Azuma, M. A New LiNbO₃-Type Polar Oxide with Closed-Shell Cations: ZnPbO₃. *J. Appl. Phys.* **2015**, *118*, 094103.
- (42) Mori, D.; Tanaka, K.; Saitoh, H.; Kikegawa, T.; Inaguma, Y. Synthesis, Direct Formation under High Pressure, Structure, and Electronic Properties of LiNbO₃-type Oxide PbZnO₃. *Inorg. Chem.* **2015**, *54*, 11405–11410.
- (43) Glazer, A. M. The Classification of Tilted Octahedra in Perovskites. *Acta Crystallogr. Sect. B* **1972**, *28*, 3384–3392.
- (44) Woodward, P. M. Octahedral Tilting in Perovskites. I. Geometrical Considerations. *Acta Crystallogr. Sect. B* **1997**, *53*, 32–43.
- (45) Megaw, H. D. A Note on the Structure of Lithium Niobate, LiNbO₃. *Acta Crystallogr. Sect. A* **1968**, *24*, 583–588.
- (46) Kubel, F.; Schmid, H. Structure of a Ferroelectric and Ferroelastic Monodomain Crystal of the Perovskite BiFeO₃. *Acta Crystallogr. Sect. B* **1990**, *46*, 698–702.
- (47) Mitchell, R. H. *Perovskites: Modern and Ancient*, Almaz Press; Ontario, 2002.
- (48) Li, M.-R.; Retuerto, M.; Walker, D.; Sarkar, T.; Stephens, P. W.; Mukherjee, S.; Dasgupta, T. S.; Hodges, J. P.; Croft, M.; Grams, C. P.; Hemberger, J.; Sánchez-Benítez, J.; Huq, A.; Saouma, F. O.; Jang, J. I.; Greenblatt, M. Magnetic-Structure-Stabilized Polarization in an Above-Room-Temperature Ferrimagnet. *Angew. Chem. Int. Ed.* **2014**, *53*, 10774–10778.
- (49) Li, M.-R.; Croft, M.; Stephens, P. W.; Ye, M.; Vanderbilt, D.; Retuerto, M.; Deng, Z.; Grams, C. P.; Hemberger, J.; Hadermann, J.; Li, W.-M.; Jin, C.-Q.; Saouma, F. O.; Jang, J. I.; Akamatsu, H.; Gopalan, V.; Walker, D.; Greenblatt, M. Mn₂FeWO₆: A New Ni₃TeO₆-Type Polar and Magnetic Oxide. *Adv. Mater.* **2015**, *27*, 2177–2181.
- (50) Dzyaloshinsky, I. A Thermodynamic Theory of “weak” Ferromagnetism of Antiferromagnetics. *J. Phys. Chem. Solids.* **1958**, *4*, 241–255.
- (51) Moriya, T. Anisotropic Superexchange Interaction and Weak Ferromagnetism. *Phys. Rev.* **1960**, *120*, 91–98.
- (52) Fennie, C. J. Ferroelectrically Induced Weak Ferromagnetism by Design. *Phys. Rev. Lett.* **2008**, *100*, 167203.
- (53) Geller, S.; Wood, E. A. Crystallographic Studies of Perovskite-Like Compounds. I. Rare Earth Orthoferrites and YFeO₃, YCrO₃, YAlO₃. *Acta Crystallogr.* **1956**, *9*, 563–568.
- (54) Marezio, M.; Remeika, J. P.; Dernier, P. D. The Crystal Chemistry of the Rare Earth Orthoferrites. *Acta Crystallogr. Sect. B* **1970**, *26*, 2008–2022.
- (55) Shannon, R. D. Revised Effective Ionic Radii and Systematic Studies of Interatomic Distances in Halides and Chalcogenides. *Acta Crystallogr. Sect. A* **1976**, *32*, 751–767.
- (56) Giaquinta, D. M.; Davis, W. M.; Zur Loye H.-C. Structure of Indium Iron Oxide. *Acta Crystallogr. Sect. C* **1994**, *50*, 5–7.
- (57) Prewitt, C. T.; Shannon, R. D.; Rogers, D. B.; Sleight, W. W. C Rare Earth Oxide-Corundum Transition and Crystal Chemistry of Oxides Having the Corundum Structure. *Inorg. Chem.* **1969**, *8*, 1985–1993.
- (58) Shannon, R. D. New High Pressure Phases Having the Corundum Structure. *Solid State Commun.* **1966**, *4*, 629–630.
- (59) Rietveld, H. M. A Profile Refinement Method for Nuclear and Magnetic Structures. *J. Appl. Crystallogr.* **1969**, *2*, 65–71.
- (60) Rodríguez-Carvajal, J. Recent Advances in Magnetic Structure Determination by Neutron Powder Diffraction. *Phys. B: Condens Matter* **1993**, *192*, 55–69.
- (61) Ida, T. Efficiency in the Calculation of Absorption Corrections for Cylinders. *J. Appl. Crystallogr.* **2010**, *43*, 1124–1125.
- (62) Utsumi, W.; Funakoshi, K.; Katayama, Y.; Yamakata, M.; Okada, T.; Shimomura, O. High-Pressure Science with a Multi-Anvil Apparatus at SPring-8. *J. Phys.: Condens. Matter* **2002**, *14*, 10497–10504.
- (63) Akimoto, S.; Manghnani, M. H. *High-Pressure Research in Geophysics*; Center for Academic Publications Japan, Tokyo, Japan, 1982.
- (64) Chapon, L. C.; Manuel, P.; Radaelli, P. G.; Benson, C.; Perrott, L.; Ansell, S.; Rhodes, N. J.; Raspino, D.; Duxbury, D.; Spill, E.; Norris, J. The New Powder and Single Crystal Magnetic Diffractometer on the Second Target Station. *Neutron News* **2011**, *22*, 22–25.
- (65) Momma, K.; Izumi, F. VESTA 3 for Three-Dimensional Visualization of Crystal, Volumetric and Morphology Data. *J. Appl. Crystallogr.* **2011**, *44*, 1272–1276.
- (66) Blöchl, P. E. Projector Augmented-Wave Method. *Phys. Rev. B* **1994**, *50*, 17953.
- (67) Kresse, G.; Joubert, D. From Ultrasoft Pseudopotentials to the Projector Augmented-Wave Method. *Phys. Rev. B* **1999**, *59*, 1758.
- (68) Perdew, J. P.; Ruzsinszky, A.; Csonka, G. I.; Vydrov, O. A.; Scuseria, G. E.; Constantin, L. A.; Zhou, X.; Burke, K. Restoring the Density-Gradient Expansion for Exchange in Solids and Surfaces. *Phys. Rev. Lett.* **2008**, *100*, 136406.
- (69) Kresse, G.; Hafner, J. Ab Initio Molecular Dynamics for Open-Shell Transition Metals. *Phys. Rev. B* **1993**, *48*, 13115.
- (70) Kresse, G.; Furthmüller, J. Efficient Iterative Schemes for Ab Initio Total-Energy Calculations Using a Plane-Wave Basis Set. *Phys. Rev. B* **1996**, *54*, 11169.
- (71) Resta, R.; Posternak, M.; Baldereschi, A. Towards a Quantum Theory of Polarization in Ferroelectrics: The Case of KNbO₃. *Phys. Rev. Lett.* **1993**, *70*, 1010.
- (72) Veithen, M.; Ghosez, Ph. First-Principles Study of the Dielectric and Dynamical Properties of Lithium Niobate. *Phys. Rev. B* **2002**, *65*, 214302.
- (73) Brown I. D.; Altermatt, D. Bond-Valence Parameters Obtained from a Systematic Analysis of the Inorganic Crystal Structure Database. *Acta Crystallogr. Sect. B* **1985**, *41*, 244–247; in this work, BVS was calculated using the following parameters: $b_0=0.37$ for all atoms, $r_0=1.902$ for In, and $r_0=1.759$ for Fe.
- (74) Hsu, R.; Maslen, E. N.; Boulay, D. D.; Ishizawa, N. Synchrotron X-ray Studies of LiNbO₃ and LiTaO₃. *Acta Crystallogr. Sect. B* **1997**, *53*, 420–428.
- (75) Halasyamani, P. S.; Poeppelmeier, K. R. Noncentrosymmetric Oxides. *Chem. Mater.* **1998**, *10*, 2753–2769.
- (76) Ghosez, Ph.; Michenaud, J.-P.; Gonze, X. Dynamical Atomic Charges: The Case of ABO₃ Compounds. *Phys. Rev. B* **1998**, *58*, 6224.
- (77) Neaton, J. B.; Ederer, C.; Waghmare, U. V.; Spaldin, N. A.; Rabe, K. M. First-Principles Study of Spontaneous Polarization in Multiferroic BiFeO₃. *Phys. Rev. B* **2005**, *71*, 014113.
- (78) Ravindran, P.; Vidya, R.; Kjekshus, A.; Fjellvåg, H.; Eriksson, O. Theoretical Investigation of Magnetoelectric Behavior in BiFeO₃. *Phys. Rev. B* **2006**, *74*, 224412.
- (79) Belik, A. A.; Matsushita, Y.; Tanaka, M.; Takayama-Muromachi, E. Crystal Structures and Properties of Perovskites ScCrO₃ and InCrO₃ with Small Ions at the A Site. *Chem. Mater.* **2012**, *24*, 2197–2203.

- (80) Yi, W.; Liang, Q.; Matsushita, Y.; Tanaka, M.; Belik, A. A. High-Pressure Synthesis, Crystal Structure, and Properties of $\text{In}_2\text{NiMnO}_6$ with Antiferromagnetic Order and Field-Induced Phase Transition. *Inorg. Chem.* **2013**, *52*, 14108–14115.
- (81) Belik, A. A.; Matsushita, Y.; Tanaka, M.; Takayama-Muromachi, E. High-Pressure Synthesis, Crystal Structures, and Properties of ScRhO_3 and InRhO_3 Perovskites. *Inorg. Chem.* **2013**, *52*, 12005–12011.
- (82) Keune, W.; Date, S. K.; Dézsi, I.; Gonser, U. Mössbauer-Effect Study of Co^{57} and Fe^{57} Impurities in Ferroelectric LiNbO_3 . *J. Appl. Phys.* **1975**, *46*, 3914–3924.
- (83) Eibschütz, M.; Shtrikman, S.; Treves, D. Mössbauer Studies of Fe^{57} in Orthoferrites. *Phys. Rev.* **1967**, *156*, 562–577.
- (84) Petricek, V.; Dusek, M.; Palatinus, L. Crystallographic Computing System JANA2006: General Features. *Z. Kristallogr.* **2014**, *229*, 345–352.
- (85) Arévalo-López, A. M.; Attfield, J. P. Weak Ferromagnetism and Domain Effects in Multiferroic LiNbO_3 -type MnTiO_3 -II. *Phys. Rev. B* **2013**, *88*, 104416.
- (86) Blaauw, C.; Van der Woude, F. Magnetic and Structural Properties of BiFeO_3 . *J. Phys. C: Solid State Phys.* **1973**, *6*, 1422–1431.
- (87) Lebeugle, D.; Colson, D.; Forget, A.; Viret, M. Very Large Spontaneous Electric Polarization in BiFeO_3 Single Crystals at Room Temperature and Its Evolution under Cycling Fields. *Appl. Phys. Lett.* **2007**, *91*, 022907.
- (88) Atanasov, M.; Reinen, D. Density Functional Studies on the Lone Pair Effect of the Trivalent Group (V) Elements: I. Electronic Structure, Vibronic Coupling, and Chemical Criteria for the Occurrence of Lone Pair Distortions in AX_3 Molecules (A=N to Bi; X=H, and F to I). *J. Phys. Chem. A* **2001**, *105*, 5450–5467.
- (89) Spaldin, N. A. A Beginner's Guide to the Modern Theory of Polarization. *J. Solid State Chem.* **2012**, *195*, 2–10.
- (90) Xiang, H. J. Origin of Polar Distortion in LiNbO_3 -type “Ferroelectric” Metals: Role of A-site Instability and Short-Range Interactions. *Phys. Rev. B*, **2014**, *90*, 094108.
- (91) Ederer, C.; Spaldin, N. A.; Weak Ferromagnetism and Magnetoelectric Coupling in Bismuth Ferrite. *Phys. Rev. B* **2005**, *71*, 060401(R).
- (92) Heron, J. T.; Bosse, J. L.; He, Q.; Gao, Y.; Trassin, M.; Ye, L.; Clarkson, J. D.; Wang, C.; Liu, Jian; Salahuddin, S.; Ralph, D. C.; Schlom, D. G.; Iniguez, J.; Huey, B. D.; Ramesh, R. Deterministic Switching of Ferromagnetism at Room Temperature Using an Electric Field. *Nature* **2014**, *516*, 370–373.
- (93) Yang, Y.; Iniguez, J.; Mao, A.-J.; Bellaiche, L. Prediction of a Novel Magnetoelectric Switching Mechanism in Multiferroics. *Phys. Rev. Lett.* **2014**, *112*, 057202.

Insert Table of Contents artwork here

